GFZ
Helmholtz-Zentrum
POTSDAM

Originally published as:

Teshebaeva, K., Echtler, H., Bookhagen, B., Strecker, M. R. (2019): Deep-seated gravitational slope deformation (DSGSD) and slow moving landslides in the southern Tien Shan Mountains: new insights from InSAR, tectonic, and geomorphic analysis. - *Earth Surface Processes and Landforms*, *44*, 12, pp. 2333—2348.

DOI: http://doi.org/10.1002/esp.4648

EARTH SURFACE PROCESSES AND LANDFORMS
Earth Surf. Process. Landforms **44**, 2333–2348 (2019)
© 2019 The Authors. Earth Surface Processes and Landforms Published by John Wiley & Sons Ltd
Published online 17 June 2019 in Wiley Online Library
(wileyonlinelibrary.com) DOI: 10.1002/esp.4648

Deep-seated gravitational slope deformation (DSGSD) and slow-moving landslides in the southern Tien Shan Mountains: new insights from InSAR, tectonic and geomorphic analysis

Kanayim Teshebaeva,[1,2]* Helmut Echtler,[2,3] Bodo Bookhagen[3] and Manfred Strecker[3]
[1] Free University of Amsterdam, De Boelelaan, 1083 HV, Amsterdam, Netherlands
[2] GFZ German Research Centre for Geosciences, Telegrafenberg, 14473 Potsdam, Germany
[3] Institute of Earth and Environmental Sciences, Potsdam University, 14476 Potsdam, Germany

Received 9 March 2018; Revised 15 April 2019; Accepted 2 May 2019

*Correspondence to: Kanayim Teshebaeva, Free University of Amsterdam, De Boelelaan, 1083 HV Amsterdam, Netherlands. E-mail: kanayim@gmail.com
This is an open access article under the terms of the Creative Commons Attribution License, which permits use, distribution and reproduction in any medium, provided the original work is properly cited.

ESPL
Earth Surface Processes and Landforms

ABSTRACT: We investigated deep-seated gravitational slope deformation (DSGSD) and slow mass movements in the southern Tien Shan Mountains front using synthetic aperture radar (SAR) time-series data obtained by the ALOS/PALSAR satellite. DSGSD evolves with a variety of geomorphological changes (e.g. valley erosion, incision of slope drainage networks) over time that affect earth surfaces and, therefore, often remain unexplored. We analysed 118 interferograms generated from 20 SAR images that covered about 900 km^2. To understand the spatial pattern of the slope movements and to identify triggering parameters, we correlated surface dynamics with the tectono-geomorphic processes and lithologic conditions of the active front of the Alai Range. We observed spatially continuous, constant hillslope movements with a downslope speed of approximately 71 mm $year^{-1}$ velocity. Our findings suggest that the lithological and structural framework defined by protracted deformation was the main controlling factor for sustained relief and, consequently, downslope mass movements. The analysed structures revealed integration of a geological/structural setting with the superposition of Cretaceous–Paleogene alternating carbonatic and clastic sedimentary structures as the substratum for younger, less consolidated sediments. This type of structural setting causes the development of large-scale, gravity-driven DSGSD and slow mass movement. Surface deformations with clear scarps and multiple crest lines triggered planes for large-scale deep mass creeps, and these were related directly to active faults and folds in the geologic structures. Our study offers a new combination of InSAR techniques and structural field observations, along with morphometric and seismologic correlations, to identify and quantify slope instability phenomena along a tectonically active mountain front. These results contribute to an improved natural risk assessment in these structures. © 2019 The Authors. Earth Surface Processes and Landforms Published by John Wiley & Sons Ltd

KEYWORDS: interferometric SAR (InSAR); small baseline subset (SBAS); gravity-driven slope deformation; landslide; tectonic geomorphology; Tien Shan Mountains

Introduction

Voluminous landslides represent a major natural hazard in tectonically active and high-relief regions and, therefore, require accurate detection and monitoring to mitigate hazardous changes in slope conditions (Keefer, 1984; Hermanns *et al.*, 2001; Crosta *et al.*, 2013). Landslides occur commonly along mountain fronts with distinct topographic relief, which pose significant geological hazards and risks for communities along mountain fronts and in valleys (Havenith *et al.*, 2006; Strom, 2013; Qiu *et al.*, 2016). Mountain fronts with slow-moving landslide masses are often affected by a sudden acceleration of downhill motion and rapid displacement of material. Deep-seated gravitational slope deformation (DSGSD) is mountain slope deformation of steep, high mountain slopes, manifested by scarps and cracks, but lacking a defined rupture surface and slow movement rates (Hungr *et al.*, 2014). DSGDS is commonly observed together with nested landslides, and temporal succession of DSGSD–landslide has been proposed (Ambrosi and Crosta, 2006; Agliardi *et al.*, 2013; Capitani *et al.*, 2013; Hungr *et al.*, 2014). Understanding hillslope processes and failure conditions in high mountain environments, which include regional geotechnical assessments and hillslope-stabilization strategies, is vital for an efficient governance of disaster preparedness in communities at risk. This has become increasingly important given the high mortality rates and high costs associated with landslides (Klose *et al.*, 2014).

The environmental impacts of both deep-seated (e.g. protracted deformation of slopes, such as in the Tien Shan) and rapid mass movements have been recognized for a long

time (Dikau *et al.*, 1996; Agliardi *et al.*, 2001; Galadini, 2006; Strom and Korup, 2006; Gori *et al.*, 2014; Strom, 2015). Studies are increasingly using advanced methodology and higher-quality data from satellites. For example, landslide studies are increasingly using differential SAR interferometry techniques to monitor the spatiotemporal characteristics of DSGSG and slow-moving landslides (Hilley *et al.*, 2004; Ambrosi and Crosta, 2006; Colesanti and Wasowski, 2006). Such analyses help to assess the roles of unsteady slope conditions, hydrologic changes and seismicity in generating mass movements. However, we require improved understanding of such movements with regard to structural predispositions of mountain fronts and active tectonic structures that may help to explain the locations of large slope failures and their geometry in the near future. In addition, it is difficult to differentiate these tectonic aspects from climate-driven forcing of landslides or changes in landslide velocity in the case of slowly moving rock masses.

Hillslope instabilities and frequent mass movements are one of the most prominent manifestations of the interplay among active tectonism, deformation, surface uplift and climate-driven surface processes along tectonically active fronts of the Tien Shan Mountains and adjacent Pamir Mountains (Biske *et al.*, 1996; Arrowsmith and Strecker, 1999; Strecker *et al.*, 2003; Burtman, 2006). To date, systematic research on DSGSD in the Tien Shan Mountains is underexplored and requires identification and monitoring of locations prone to repeated slope movements and landslides.

This study focuses on areas of active tectonism and landslides in the southern Tien Shan Mountains (Figure 1). The study area is located in the south and east of the seismically active Fergana Basin and includes protracted mass movement-affected mountain fronts. The flanks of the Alai Range in this region record numerous voluminous landslides each year that have affected the morphology of range fronts

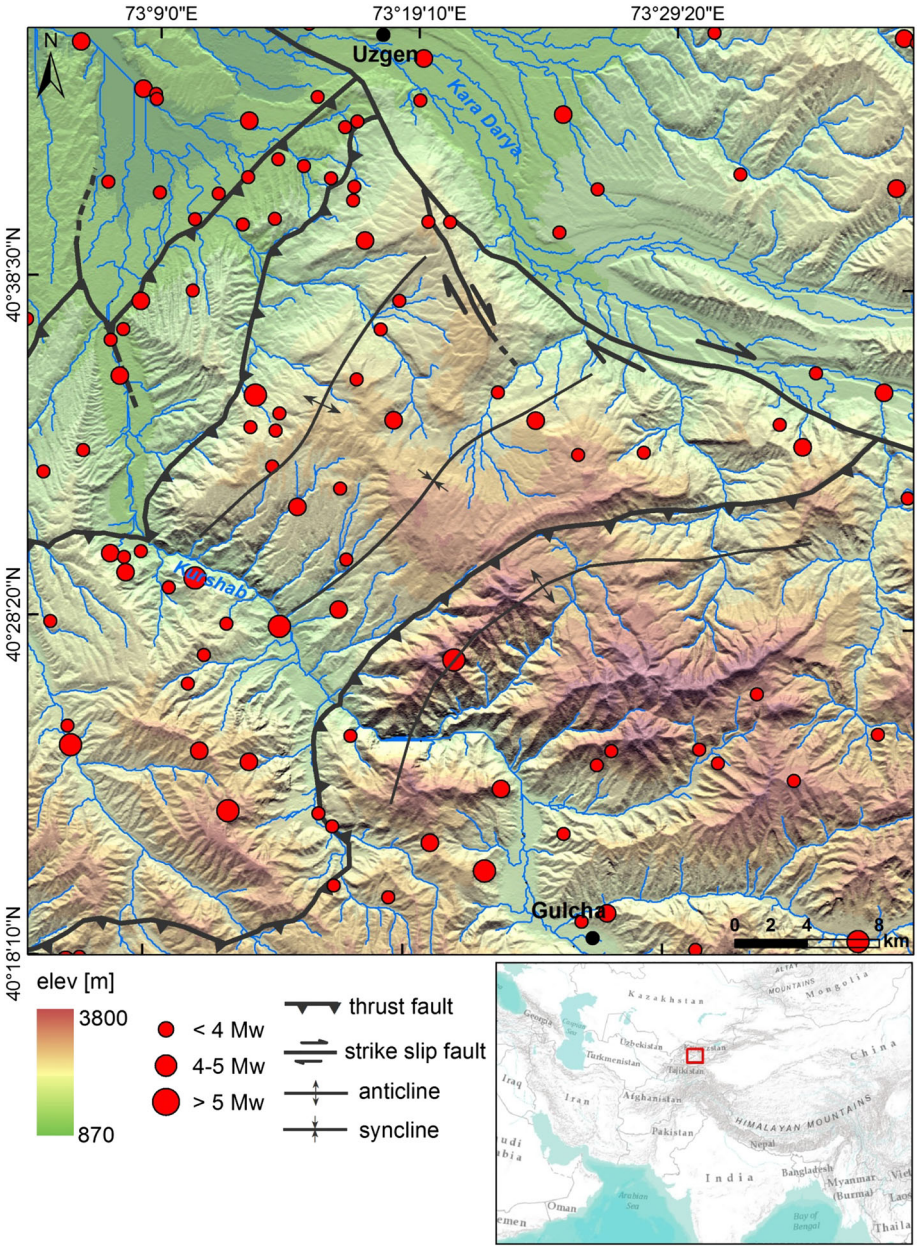

Figure 1. Geographic location of the study area in the southern Kyrgyz Tien Shan (see inset). Main geologic structures modified after Chediya (1986); map is based on SRTM topography with 30 m resolution. Red circles denote instrumentally recorded earthquakes from the NEIC catalogue and regional seismic network of IRIS for the period between 1973 and 2015; magnitudes of earthquakes scale with diameter of circle. [Colour figure can be viewed at wileyonlinelibrary.com]

© 2019 The Authors. Earth Surface Processes and Landforms Published by John Wiley & Sons Ltd

and their piedmont regions (Roessner *et al.*, 2005; Strom and Korup, 2006; Danneels *et al.*, 2008; Havenith *et al.*, 2010). Deep-reaching and slow-moving mass movements are ubiquitous phenomena in intermountain valleys and along fault-controlled mountain fronts in the Alai Range of the Tien Shan (Wetzel *et al.*, 2000; Havenith *et al.*, 2010; Teshebaeva *et al.*, 2015). Typically, range fronts exhibit multiple cuspate break-off scarps, extensional, slope-parallel trenches and evidence of rotational movements. The toe areas of hummocky slopes along range fronts have apparently displaced the fluvial network, which suggests an efficient, perhaps protracted and sustained, mechanism of mass transfer from the hillslopes to the fluvial channel systems. These features altogether make this region a good setting to decode the roles of different forcing mechanisms on mass movements and their temporal behaviour (Chediya, 1986; Wetzel *et al.*, 2000; Abdrakhmatov *et al.*, 2003; Teshebaeva *et al.*, 2015). We hypothesize that the active tectonics and uplift in the Tien Shan are the main forcing mechanisms to sustain the necessary gravitational forces of slope deformation and form DSGSD along the Alai Range.

Here we present an innovative and quantitative approach for DSGSD detection and assessment that uses time-series InSAR data with tectonic and geomorphic analyses. We tested this approach in the southern Tien Shan mountain range. We calculated the movement rate using the differential SAR interferometry small baseline subset (SBAS) technique. We also integrated seismological data with regional intensity gradients to support our observations and analysis on the main controlling parameters of the surface dynamics that we studied.

Geologic and Geomorphologic Setting of the Southern Tien Shan and Alai Range

The study area is situated on the north-facing flank of the Alai Range, where the sedimentary strata of the Fergana Basin are incorporated into the active orogenic wedge of the Alai–Pamir system of north-vergent thrusts (Figure 1). The Alai Range is part of the Tien Shan active orogen in Central Asia. Rocks exposed in the Alai Range mainly consist of Late Paleozoic orogenic metamorphic basement, and folded Mesozoic and Tertiary sedimentary cover units with shallow marine and terrestrial sediments. The oldest sedimentary cover units include Jurassic terrestrial clastics and coal layers, followed by Late Cretaceous to Eocene marine limestones (Cobbold *et al.*, 1992; Biske *et al.*, 1996). Oligocene sedimentary strata are superseded by fine-

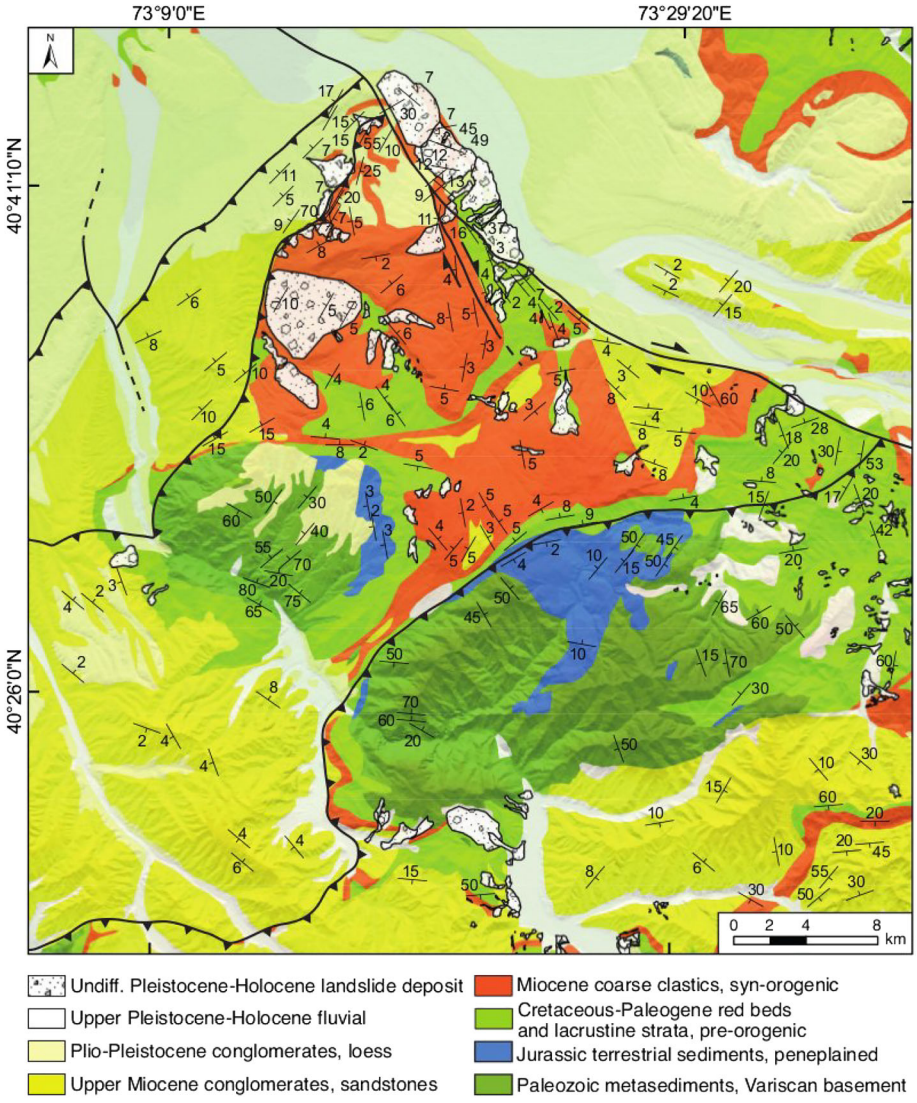

Figure 2. Detailed geologic, tectonic and structural map of the study area compiled from 1:50 000 and 1:200 000 geological maps of the Kyrgyz Geological Agency (1958, 1985) and field observations. Landslide deposits were mapped based on optical satellite remote sensing data and field observations (Wetzel *et al.*, 2000). [Colour figure can be viewed at wileyonlinelibrary.com]

© 2019 The Authors. Earth Surface Processes and Landforms Published by John Wiley & Sons Ltd

grained clay and evaporite-bearing lacustrine and shallow marine units, which are covered by coarsening-upward Late Oligocene and Neogene strata that record the onset and the tectonic processes associated with the India–Eurasia collision (Molnar and Tapponnier, 1975).

To the south, the Paleozoic basement of the Alai Range forms the substratum of the intra-mountain Alai Valley, which is located immediately north of the north-vergent thrust belt of the Pamir (Trans Alai)–Tien Shan collision zone between the northwestern Indian indenter and Eurasia (Burtman and Molnar, 1993). The south-dipping, range-bounding faults of the Alai Range have been active tectonically since the Oligocene (Coutand *et al.*, 2002; Sobel *et al.*, 2011), and they are considered to be an integral part of the Pamir orogenic wedge (Burtman, 2006; Teshebaeva *et al.*, 2014). The present-day convergence rate between India and Eurasia using space-geodetic measurements is approximately 25 mm year^{-1} (Reigber *et al.*, 2001; Zubovich *et al.*, 2010). The Pamir thrust system integrates about half of that convergence at 12 mm year^{-1} (Zubovich *et al.*, 2010), which is compatible with geologically determined shortening rates on millennial timescales (Arrowsmith and Strecker, 1999).

The northern mountain front of the Alai Range in the area of Uzgen (Figures 1 and 2) records active uplift, folding, north-vergent thrusting and reverse faulting. The Alai Mountain front between the Fergana lowland and the Gulcha high-relief fold-and-thrust system (Figures 1 and 2) comprises an area of about 3000 km^2 with a topographic gradient ranging from 870 to 3800 m above sea level. This area includes the Kara Darya River basin and is divided into many hydrographic sub-basins. The drainage network is clearly controlled by the active structures of the orogenic wedge (Chediya, 1986; Bazhenov *et al.*, 1999; Burtman, 2006). Thrusts, such as top-to-N thrusts and top-to-S back-thrusts, dextral (transpressional) and NW–SE-striking strike–slip faults dominate the fold-and-thrust belt geometry (Figures 1 and 2). These strike–slip zones may constitute transfer structures that link different thrust faults kinematically in a field of general N–S-oriented shortening. Fold axes from the actively deforming Neogene to Quaternary sedimentary formations (Figures 1 and 2) and the strike of the related thrust and reverse faults generally trend 45–60° N. The DSGSD studied here is situated along active faults and folds that integrate Late Neogene sediments and Cretaceous–Paleogene hard rock (Chediya, 1986; Biske *et al.*, 1996) (Figure 2).

Seismicity

The Alai Range of the Tien Shan Mountains is part of a region with ongoing tectonic activity, with evidence of multiple earthquake ruptures in the past (Taylor and Yin, 2009; Landgraf *et al.*, 2016), although not all range fronts and intra-mountain basins exhibit a widely distributed high level of current seismicity (Haberland *et al.*, 2011; Feld *et al.*, 2015). In general, earthquake focal mechanisms are compatible with the kinematics of the regionally characteristic reverse fault, thrust fault and displacements along strike–slip faults. Regional structures and earthquake focal mechanisms are compatible with a NNW–SSE-oriented compressional stress field (Cobbold *et al.*, 1992; Buslov *et al.*, 2007).

The distribution of shallow seismicity clearly lacks a well-defined deformation front because the earthquakes are distributed differently in time and space compared with the overall tectonic deformation pattern of the region (Ghose *et al.*, 1998; Sycheva *et al.*, 2008; Schurr *et al.*, 2014). The National Earthquake Information Center (NEIC) of the US Geological Survey and the regional seismic network of Incorporated Research Institutions for Seismology (IRIS) recorded numerous earthquakes during 1973–2015, with Mw $>$ 3 in Kyrgyzstan. All the recorded events were crustal earthquakes with hypocentre depths of 10–25 km (Figure 1).

Climatic conditions

The climate of the region is semi-arid with average precipitation of 350–600 mm year^{-1} (Yerokhin, 1999). The annual precipitation regime has two maxima, one in spring (April and May) and a less pronounced one in autumn (October and November). The study area is snow covered during winter, with a thickness of 20–100 cm, depending on elevation and exposition. The average temperature is about −10°C in winter (December to February) and +24°C in summer (June to August) (Duethmann *et al.*, 2013).

Landslides and surface deformation.

Landslides occur frequently in the southern Tien Shan Mountains. The NEIC and IRIS cumulatively recorded ~4500 landslide events in the region during 1969–2010. Characteristically, landslides occurred along mountain fronts within an elevation of 700 and 2000 m above sea level. Protracted mountain building has created pronounced topographic contrasts between ranges and valley bottoms. This geomorphic setting, together with landslide-prone unconsolidated sedimentary rocks (Chediya, 1986), was conducive to deep-reaching rotational landslides (Roessner *et al.*, 2005). Findings suggest that deep-reaching landslides affected the bedrock to depths of $>$15 m (field observations). These mass movements were often slow, continuous movement over long periods of activity. Landslide frequency peaks between March and April and again in October (Yerokhin, 1999). The multi-date landslide inventory (Ibatulin, 2011) revealed a high degree of inter-annual variability mainly caused by changes in groundwater levels, which depended on the precipitation characteristics of the preceding winter season (Yerokhin, 1999; Danneels *et al.*, 2008). Overall, landslide events varied in size and movement rates, which included very slow-moving landslides in the area (Teshebaeva *et al.*, 2015).

The frequent occurrence of large landslides in the Tien Shan Mountains has resulted in the temporary formation of dams and diversions across river courses (Havenith *et al.*, 2006; Strom and Korup, 2006). Landslide events in the region frequently lead to extensive damage of settlements and infrastructure, and cause loss of human lives (Ibatulin, 2011). A catastrophic landslide on 22 April 2003 killed 38 people in Kara-Taryk village, located along the Kurshab River. On 27 April 2004, a landslide in the same area buried and killed 33 people, which highlighted the risk associated with landslide events in the region. Satellite remote sensing and field-based investigations of predisposing structural factors have revealed that geological and structural conditions played a major role in the spatial distribution of landslides in the Tien Shan (Roessner *et al.*, 2000, 2005; Wetzel *et al.*, 2000; Teshebaeva *et al.*, 2015). However, despite these recent advances in our understanding of landslide events in the Tien Shan Mountains, we do not know much about the very slow-moving and deep-seated landslides and their relationship with lithology, structure, climate and the region's topographic relief.

© 2019 The Authors. Earth Surface Processes and Landforms Published by John Wiley & Sons Ltd

Data and Methods

Data

We analysed 20 ascending L-band ALOS/PALSAR data items collected during February 2007–October 2010. The L-band is the transmitting and receiving microwave frequency of PALSAR. It operates at a wavelength of 23.6 cm with a 46-day cycle of temporal resolution and a 38° incidence angle. The capability of L-band to reach the ground by partially penetrating through vegetation cover to obtain information about the ground surface makes PALSAR suitable especially for mapping active deformations over large areas. We used the SRTM (Shuttle Radar Topography Mission) digital elevation model (DEM) for geomorphological analysis (Farr and Kobrick, 2000). SRTM is the C-band 3-arcsecond global elevation data at a spatial resolution of 90 m. We also used data derived from the 1:200 000 and 1:50 000 geological maps produced by the Leningrad State University in 1958 and the Kyrgyz Geological Agency in 1985.

InSAR time-series analysis.

We estimated SAR interferograms and displacement rates using Interferometry Package (ROI_PAC), the Delft Object-oriented Radar Interferometric Software (DORIS) and Stanford Method of Persistent Scatter (StaMPS) programs. Twenty raw data items were analysed and focused using the ROIPAC package (Rosen *et al.*, 2004) to create single look complex (SLC) images, and the area of interest was determined in the master image; all other images were cropped accordingly. Furthermore, we processed 20 SLC images to form 118 interferograms for the SBAS technique. Interferometric processing was performed using DORIS software (Kampes *et al.*, 2003) and the topographic phase was removed using the SRTM 3-arc second DEM. We used StaMPS software to obtain data on ground deformation using the SBAS technique of interferogram stacking (Berardino *et al.*, 2002; Hooper, 2008). The SBAS technique uses interferograms with small spatiotemporal baselines to mitigate decorrelation phenomena of the SAR data and Doppler centroid-frequency differences (Berardino *et al.*, 2002). The results of the SBAS analysis provided mean displacement-velocity maps and time-series displacements of each coherent pixel, which were analysed further at their temporal evolution. We generated a subset of small baseline interferograms with spatial (<2560 m) and temporal (<950 days) baselines to maintain better coherence. The key requirement in selecting spatial and temporal baselines is to consider nearly all of the available SAR acquisitions. After generating the small baseline subsets, StaMPS used a persistent scatterer pixel search to investigate a

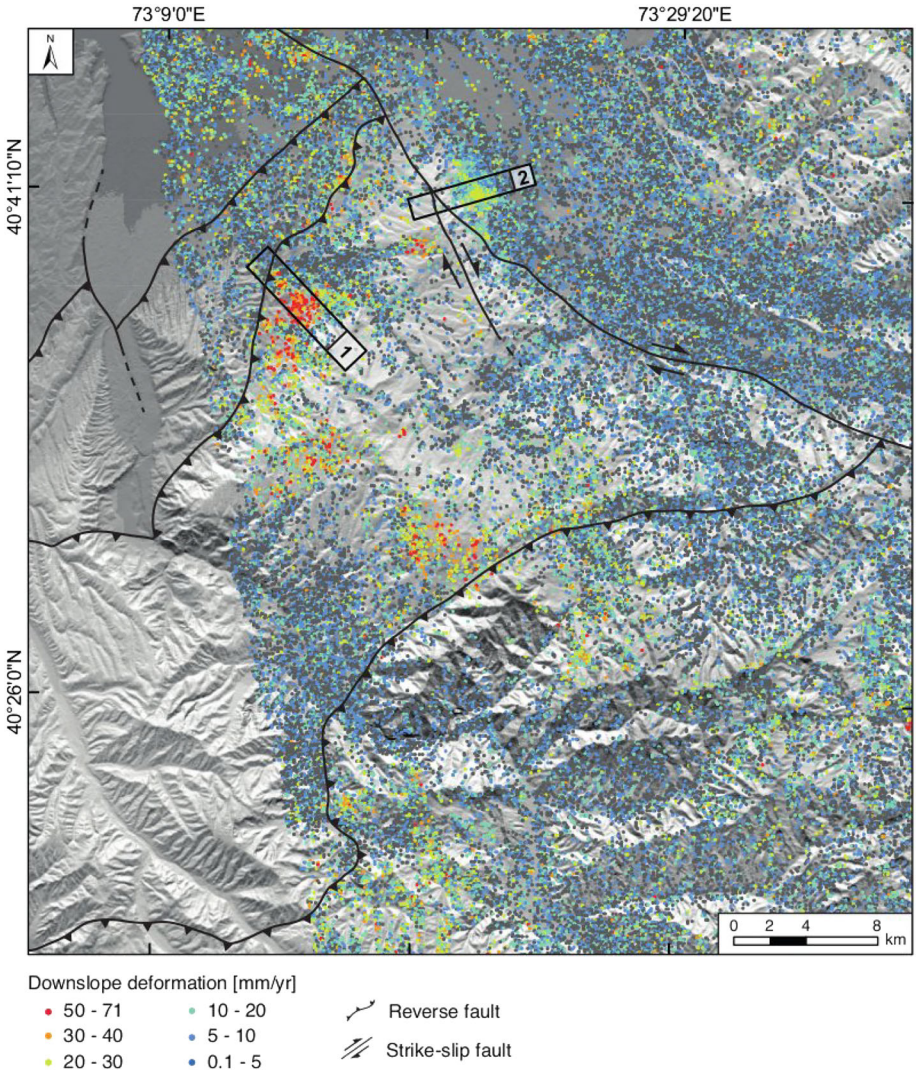

Figure 3. Results of SBAS InSAR analysis based on 118 interferograms from 20 radar scenes between 2007 and 2010. Colours show spatial pattern of downslope velocity (Vslope) rates (mm year^{-1}). Black boxes outline subsets based on hotspot cluster analyses (cf. Figure 4). [Colour figure can be viewed at wileyonlinelibrary.com]

© 2019 The Authors. Earth Surface Processes and Landforms Published by John Wiley & Sons Ltd

coherent scatterer over time. Next, we applied a standard Goldstein filter to reduce the effects of the phase noise from the generated interferograms (Goldstein and Werner, 1998). In a subsequent step, we applied three-dimensional unwrapping, which converted each ambiguous 2π cycle to absolute values of the interferometric phase and utilized the temporal information (Hooper and Zebker, 2007). This was followed by application of the SBAS 'least-squares inversion after phase-unwrapping' method to retrieve the phase with respect to the original master.

We retrieved the quality and accuracy of the processed data by calculating DEM errors, master atmosphere and orbit error from both small baseline interferograms and single master interferograms. Finally, we geocoded the data stack with azimuth 2 and range 3 looks at a spatial resolution of 25 m and obtained mean velocity displacements in the line of sight (LOS) direction during 2007–2010. To exclude any linear trends that could influence the subsequent analysis, we detrended our time-series data. We visualized the StaMPS results using viStaMPS software and exported the data into a GIS environment for further interpretation of the ground deformation (Sousa *et al.*, 2014).

The SBAS-retrieved deformation values represented the one-dimensional LOS projection of the actual movement of the Earth's surface. To overcome the differences between the ground geometry and LOS direction, we projected LOS deformation into the direction of the downslope movement. We converted the LOS velocity deformation rates into velocity deformation and downslope deformation (Vslope) (Cascini *et al.*, 2010; Zhao *et al.*, 2012). To transform LOS direction to downslope direction, we required information on the unit LOS vector and the hillslope angle. For the unit LOS vector, we used the incidence angle and flight azimuth of the satellite trajectory. In addition, we calculated hillslope angles and slope azimuths of the study area, which included the determination of hillslope and azimuth values using SRTM elevation data.

Hotspot and cluster analysis

We performed a hotspot and cluster analysis to detect areas of slow-moving landslides based on a large amount of point data. This analysis revealed spatial clusters of similar values and allowed us to identify regions that exhibited significant spatial clustering in our data. The hotspot and cluster analysis is based on two statistical approaches, the Getis–Ord Gi statistic (Getis and Ord, 2010) and kernel density estimation (Silverman, 1986). We performed hotspot analysis on the mean downslope velocity deformation. First, we calculated Getis–Ord Gi statistics for each point feature in a dataset where statistics were based on analysing the spatial pattern of each feature within the context of its neighbours. A single point feature with a high value may not be a representative measurement. The Getis–Ord Gi statistic requires that neighbours also have elevated values. To be a statistically significant hotspot, a point feature will have a high value and must be surround by other features with similar values. The local sum for a point feature and its

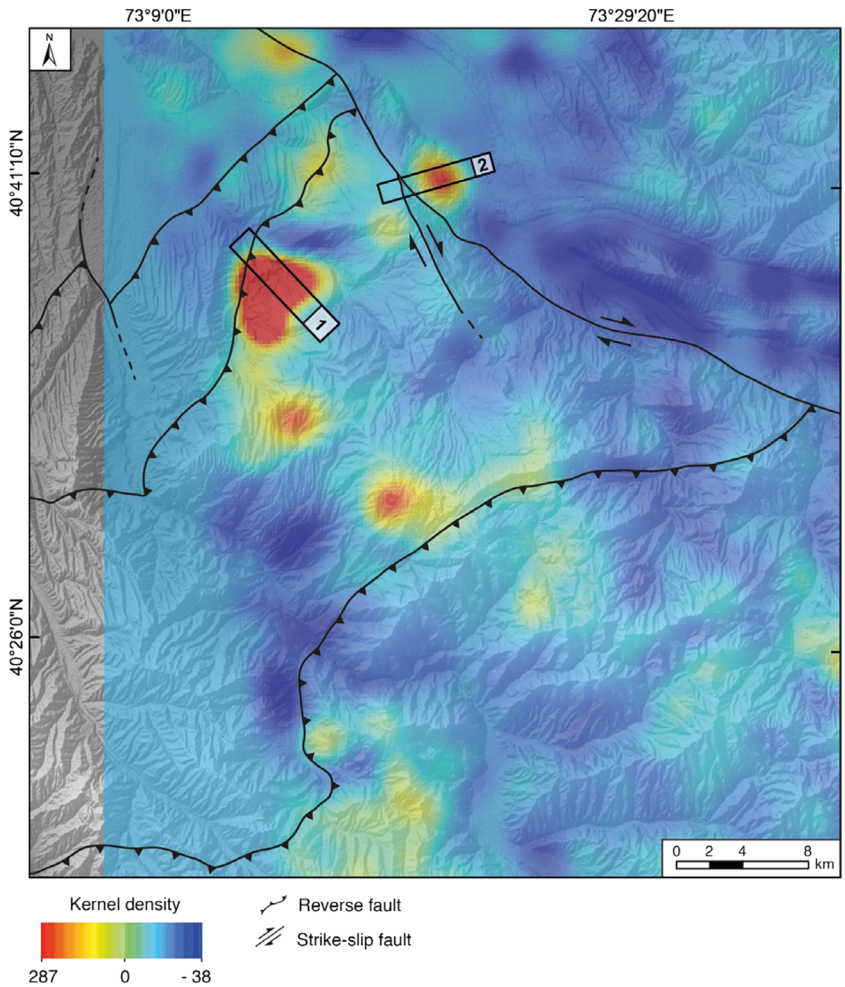

Figure 4. Hotspot cluster kernel density map showing smoothed spatial location of hotspot clusters in regions 1 and 2. Analysis highlights areas of spatially correlative regions (i.e. clusters) as high kernel density values in red. Hotspot analysis was performed on downslope velocities. [Colour figure can be viewed at wileyonlinelibrary.com]

© 2019 The Authors. Earth Surface Processes and Landforms Published by John Wiley & Sons Ltd

neighbours was compared proportionally to the sum of all features. If the local sum was different from the expected local sum, and when that difference was too large to be the result of random chance, a statistically significant *z*-score was assigned to that point. The *z*-score values indicated to us where point features with either high or low values clustered spatially. The kernel density estimator fits a smooth surface as a hotspot. The kernel density estimator is performed on downslope velocity point data by choosing derived Gi* as the weighting factor. The output was a smooth kernel density map, which converted large amounts of point data into several hotspots for better visualization.

Analysis of conformity between topographic surface and geological structures

Topographical analysis with respect to geological structures defines susceptible classes for DSGSD in selected areas. We used on-site measured geological bedding data and SRTM DEM to perform these analyses. The degree of conformity between topographic and geological surfaces was expressed as the index of the topographic/bedding-plane intersection angle (TOBIA) (Meentemeyer and Moody, 2000). When a sedimentary rock unit contained a distinct bedding plane, TOBIA was categorized into three classes (Cruden and Hu, 1996; Meentemeyer and Moody, 2000). For example, if the bedding plane dipped in the same direction as the hillslope angle, the hillslope was classified as cataclinal. If the bed dipped in the direction opposite to the hillslope, then the hillslope was classified as anaclinal (Cruden and Hu, 1996). In those cases where the azimuth of the dip direction was perpendicular to the azimuth of the hillslope direction, the slopes were referred to as orthoclinal (Meentemeyer and Moody, 2000). We defined three conformity classes using the TOBIA index: cataclinal, anaclinal and orthoclinal. These conformity classes were used to define the spatial location and distribution of the InSAR-defined, slow-moving landslides.

Results

Changes in the velocity of deformation based on InSAR measurements

The SBAS results from L-band PALSAR data recorded the location of unstable hillslopes and the downslope deformation velocity (Vslope). The Vslope displacement rates were 0–71 mm year^{-1}, making them the highest rates in the region's prior slope failures (Figure 3). The high downslope deformation rates were found mainly in the downslope vicinity of existing landslide scarps (Figure 2). We identified spatially clustered areas of high values (hotspots) and highlighted them as cluster 1 and 2, which revealed evidence of large-scale mass movements (Figure 4). The obtained downslope velocity rate was approximately 71 and 36 mm year^{-1} for hotspot cluster 1 and 2, respectively; that is, downslope velocity rates for hotspot cluster 1 were twice those of hotspot cluster 2. We analysed two profiles across hotspot clusters 1 and 2 (Figures 3 and 4). Profile 1 had a length of 7 km and transected a zone with high displacement rates (Figures 4 and 10). Profile 2 had a length of about 6 km and was located in a zone where the high deformation signal was observed across the slope for an area about 6 km wide, which was covered by several extensive landslide deposits (Figures 1, 4 and 10). Based on these profiles, we examined the relationship between the mean downslope

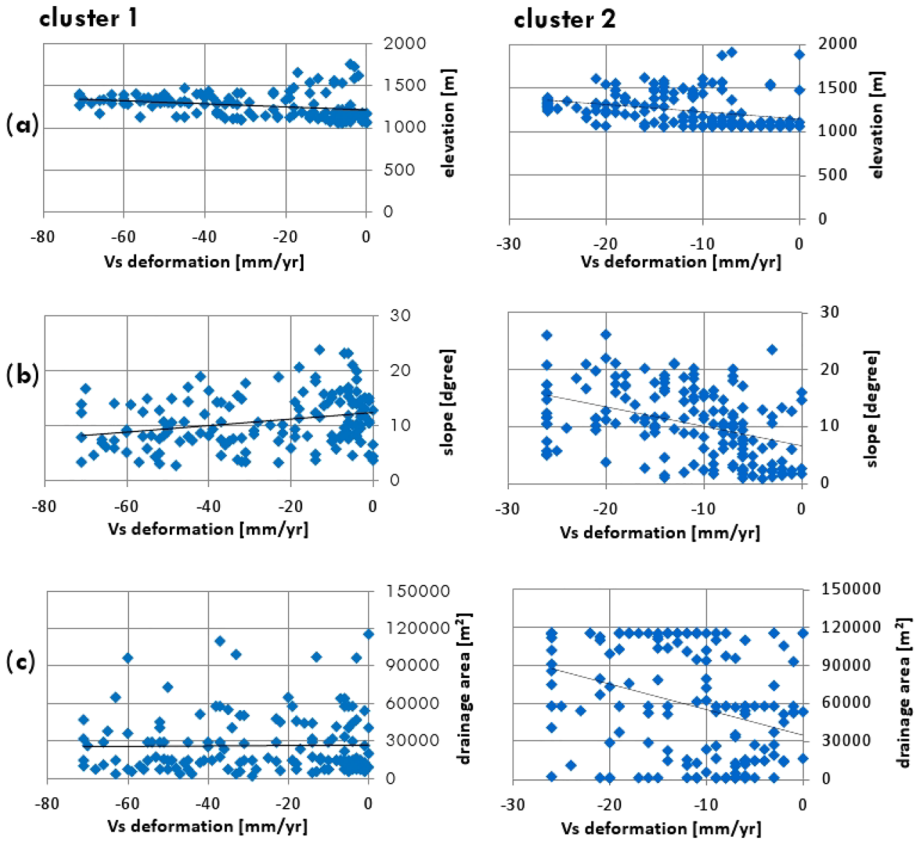

Figure 5. Downslope velocity Vslope deformation rate (mm year^{-1}) plotted against (a) elevation, (b) hillslope angle and (c) flow direction for profiles of hotspot clusters 1 and 2 (cf. Figures 3 and 4). This analysis reveals that elevation, hillslope angle and drainage area do not significantly influence downslope velocities. [Colour figure can be viewed at wileyonlinelibrary.com]

© 2019 The Authors. Earth Surface Processes and Landforms Published by John Wiley & Sons Ltd

velocity-displacement rates and topographic properties (absolute elevation, slope and flow accumulation derived from the SRTM DEM) along these profiles (Figure 5).

Downslope displacement and elevation

Plotting the observed Vslope displacement values against the absolute elevation values (Figure 5a) revealed that the observed signals of increased deformation mostly occurred in an elevation range of 1000–1500 m. Maximum elevation along slope 1 was about 2000 m, whereas slope 2 showed a slightly higher maximum elevation that ranged up to 2500 m. These profiles were characterized by a sharp lower boundary at 1000 m. These observations suggested that the detected landslide reactivations might have been facilitated by sliding planes, which were associated with folded structures along the southern Tien Shan Mountain front.

Downslope displacement and slope angle

Profile 1 showed that deformation was distributed between slope angles of 5 and 25°, whereas the lower slope values occurred in the area close to the thrust fault (Figure 1). Deformation in profile 2 was related to hillslope angles of 0–30°. The higher maximum slope values reflected the greater steepness of hotspot area 2 compared with hotspot area 1. However, the velocity-displacement rates measured in hotspot area 2 were twice as small as in hotspot area 1. There was no correlation between the hillslope angle and downslope-velocity displacement rates.

Downslope displacement and flow accumulation

The displacement values were plotted against flow accumulation (drainage area) using a logarithmic scale (Figure 5c). Hotspot 1 results suggested that the displacement was mainly related to contributing areas of up to 70 000 m^2, whereas for hotspot 2 the contributing areas were larger, with a maximum value of 120 000 m^2. The observed high deformation rates coincided spatially with the overall flow direction of the local drainage network in areas of hotspot cluster 1 (Figure 4). Deformation rates of hotspot cluster 2 were perpendicular with respect to the overall flow direction of the local drainage network, which corresponded to the strike of the dextral strike–slip fault at the eastern slope. As a result, a more advanced drainage network compared with the area of profile 2 characterized the area covered by profile 1.

Local seismic network and InSAR kernel density

Results from the kernel density analysis of InSAR data revealed that there were smoothed spatial locations of hotspot clusters in regions 1 and 2 (Figure 4). Based on IRIS network data, the regional seismicity pattern showed seismic energy release at clusters in regions 1 and 2 (Figure 6). Analysis highlights areas

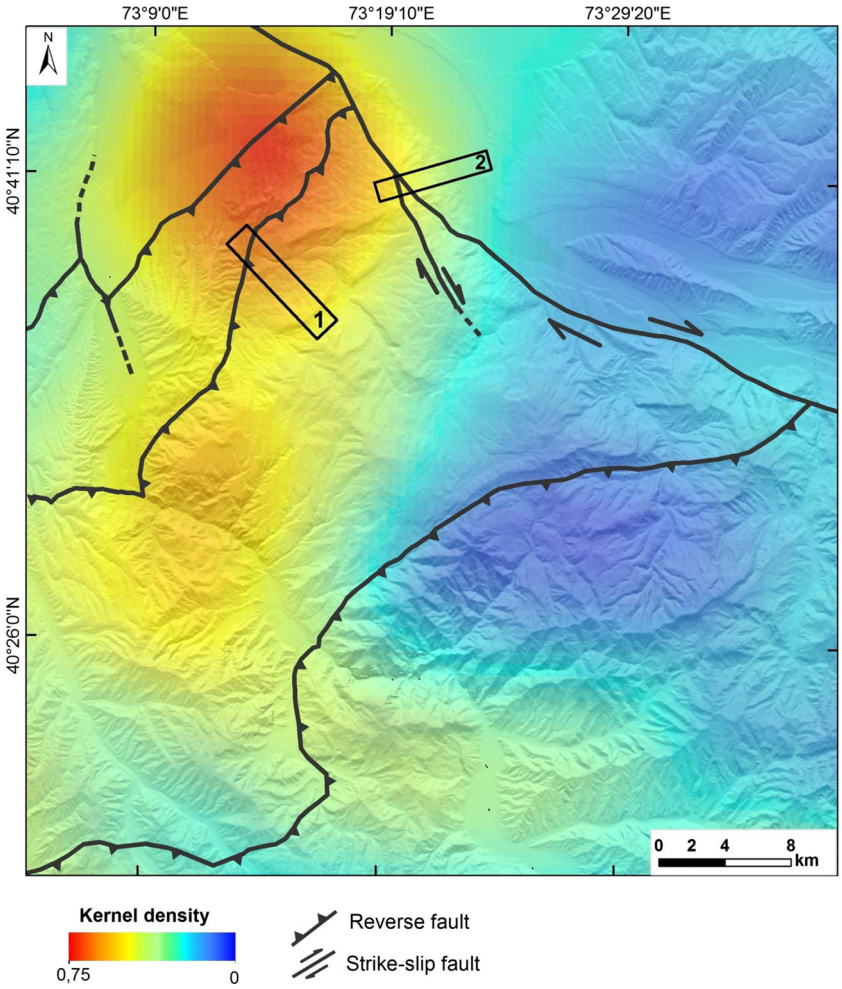

Figure 6. Kernel density inferred from regional seismic IRIS catalogue data. The regional seismicity pattern shows seismic energy release at clusters in regions 1 and 2. Analysis highlights areas of spatially correlative regions (i.e. clusters) as high kernel density values in red and correlates with InSAR-defined kernel density regions (cf. Figure 4). [Colour figure can be viewed at wileyonlinelibrary.com]

© 2019 The Authors. Earth Surface Processes and Landforms Published by John Wiley & Sons Ltd

of spatially correlative regions (i.e. clusters) as high kernel density values in red and correlates with InSAR-defined kernel density regions (Figure 4). The regional seismic energy release that correlated with InSAR clusters underlined the interaction of surface processes and tectonic strain (Figures 4 and 6).

Conformity between topographic and geological surfaces

Spatially distributed estimates of topographic/bedrock intersection angles were calculated using the categorical and continuous TOBIA models, respectively (Figures 7 and 8). By overlaying outputs from the TOBIA index and our hotspot cluster analysis, the conformity between topography/bedding planes and spatial location of slow-moving landslides was represented within each of the classified/indexed slope types (Figures 4, 7 and 8).

The slope-classification map illustrates variations in slope type as a function of different slope aspect and dip direction combinations (Figure 7). Most cataclinal slopes corresponded to northwest and west-facing sectors. Hotspot 1 in Figure 6 depicts a cataclinal slope, which was associated with a relatively gentle slope gradient, whereas the topographic slope was generally north-facing and varied from relatively gentle to steep gradients. Anaclinal slopes were typically associated with east-facing slopes and constituted a higher percentage of mapped surface (Figures 4 and 7). Anaclinal slopes typically occurred along moderately inclined northeast and east-facing hillslopes. Field observations indicated that the mapped anaclinal slopes often corresponded to outcrops of the ubiquitous Cretaceous limestones and the resistant Paleozoic rocks. Orthoclinal slopes covered the lowest percentage of mapped area in the study region (Figure 6). Due to the northeast and northwest strike of the bedding planes, orthoclinal slopes were typically common on south-facing slopes.

The TOBIA index application across the watershed (Figure 8) resulted in the same general patterns as the slope-classification map (Figure 7). The high index values corresponded to conformity among slope angles, slope aspect, dip and dip aspect, and correlated with unconsolidated Quaternary sediments. The low

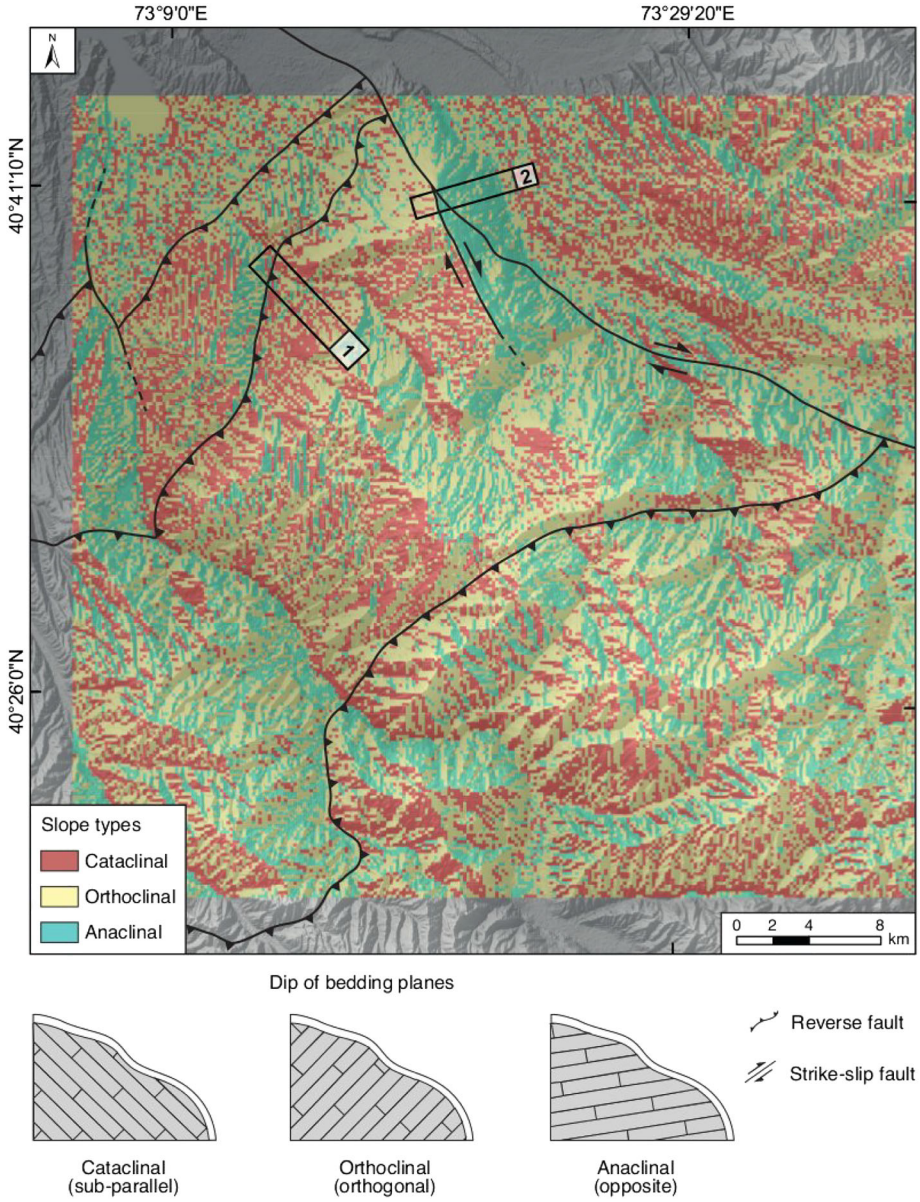

Figure 7. Slope-classification map depicting cataclinal, anaclinal and orthoclinal slopes. Slope classification based on spatially distributed estimates of slope aspect and dip-direction angles. Map indicates that cluster 1 depicts a cataclinal slope and cluster 2 depicts an anaclinal slope (cf. Figure 4). [Colour figure can be viewed at wileyonlinelibrary.com]

© 2019 The Authors. Earth Surface Processes and Landforms Published by John Wiley & Sons Ltd

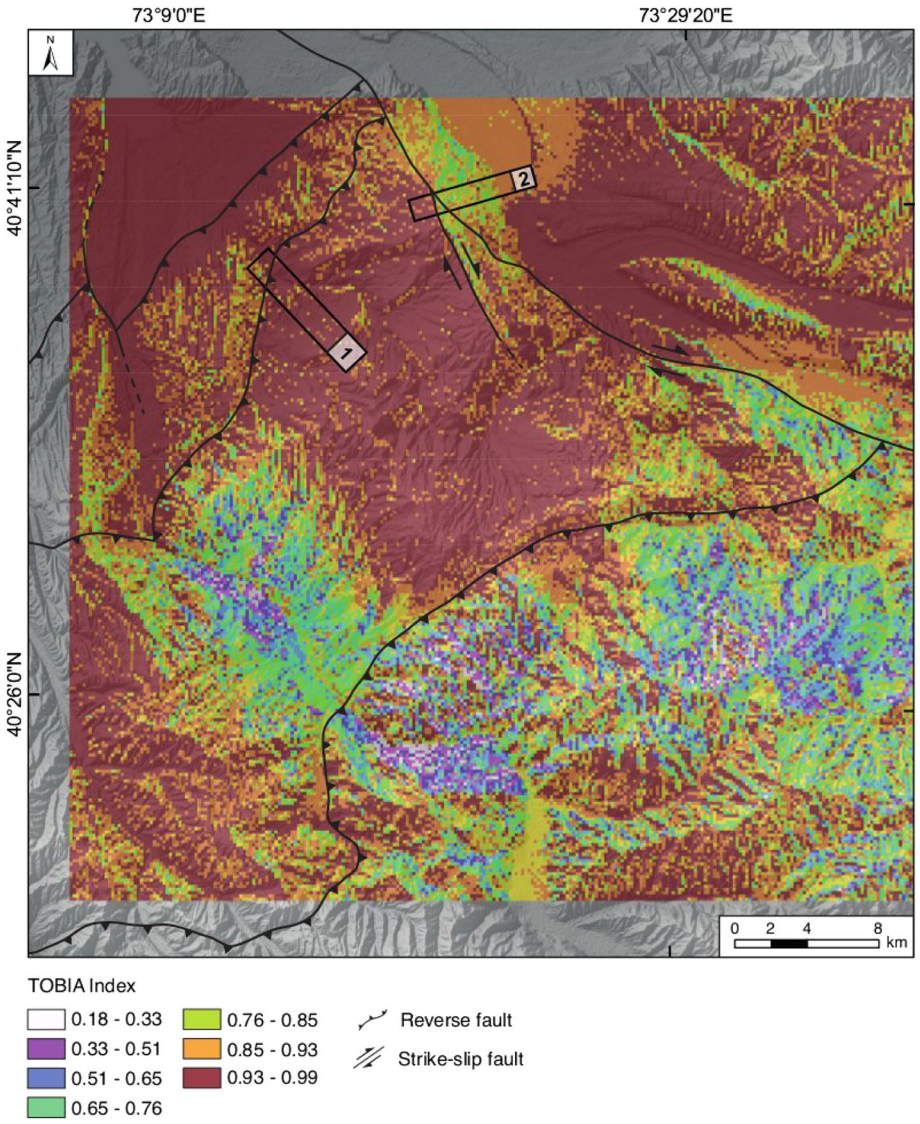

Figure 8. Topography/bedrock intersection index map (Meentemeyer and Moody, 2000) showing conformity (high index values) and non-conformity (low index values) between slope angles, slope aspect, dip and dip aspect. Cluster 1 is characterized by high conformity, while cluster 2 shows moderate conformity between topography and bedding planes. [Colour figure can be viewed at wileyonlinelibrary.com]

index values corresponded to non-conformity and correlated with Paleozoic basement rocks (Figure 2). Additionally, index values of ridges and drainages were often intermediate between cataclinal and anaclinal slopes, because they represented a transition in slope and slope aspect. The advantage of the conformity-index representation over the classification was that it permitted greater accuracy in mapping transitions of topographic/bedding plane intersection angles (Figure 9 and 10).

Discussion

Interpretation of measured slope deformation.

We observed two distinct displacement signals, clusters 1 and 2, in the study area during 2007–2010. The measured velocity deformation rates were up to 71 mm year^{-1}, which was a slow to very slow-moving slope creep (Figures 3 and 4). Clusters 1 and 2 showed significant elevational changes that were separated from the surrounding depressed areas by steep escarpments (Figures 4 and 11). In particular, contraction with tectonic uplift sustained and constantly increased the relief that sustained the development of gravity-driven deformation. Active structures and tectonic patterns affected these and were related to the inherited and ongoing mountain building processes since the Late Neogene (Biske *et al.*, 1996; Burtman, 2006). Our hypothesis is that the InSAR-derived spatial clusters with slow moving rates represented DSGSD. Despite their occurrence on high-relief slopes, displacement rates were relatively small compared with the relief of the entire slope (Agliardi *et al.*, 2001). DSGSD geomorphological indicators were in double crest lines, such as scarps and fractures. The DSGSD-induced high landslide rates, debris flow and alluvial fans have been observed along major reverse faults.

The double crest line and scarps were visible from optical data and shown in oblique 3D view profiles (Figures 9 and 10). To identify and validate the gravitational reactivation of DSGSD in the region is an important contribution. InSAR observations confirmed these data and showed congruent directions with the type of recognized deformation (i.e. DSGSD) (Figures 4 and 11). We observed velocities in downslope-directed deformation rates of up to 71 mm year^{-1}, in particular in hotspot cluster 1 (Figure 4). Cluster 2 showed lower deformation rates of about 30 mm year^{-1}.

Interestingly, similar remote sensing studies that utilized InSAR in the San Francisco Bay area detected slowly moving slopes (Hilley *et al.*, 2004). Likewise, corresponding

© 2019 The Authors. Earth Surface Processes and Landforms Published by John Wiley & Sons Ltd

observations were made in the Central Italian Apennines (Tolomei *et al.*, 2013), in the eastern Betic Cordillera of Spain (Delgado *et al.*, 2011) and in the Po River basin in northern Italy (Stramondo *et al.*, 2007).

We hypothesize that advancement of the DSGSD phenomena in the Tien Shan Mountains was due to inherited and pre-existing structural weaknesses and setting of the area. Tectonic events and local seismicity showed reactivated, fault planes that sustained the necessary gravitational creep (Figures 1 and 6). The presence of the DSGSD on the cluster 2 slope possibly contributed to the development of deep-seated landslides there (Agliardi *et al.*, 2001; Jomard *et al.*, 2014) and to the development of shallow landslides on the cluster 1 slope with less pronounced break-off scarps (Figure 11), which was also suggested by Hungr *et al.* (2014).

Implication of topographic and geologic surfaces

We observed morphological evidence of DSGSD along the two zones, which confirmed the existence of active large-scale gravity-driven processes (Figures 4, 6 and 11). The spatial

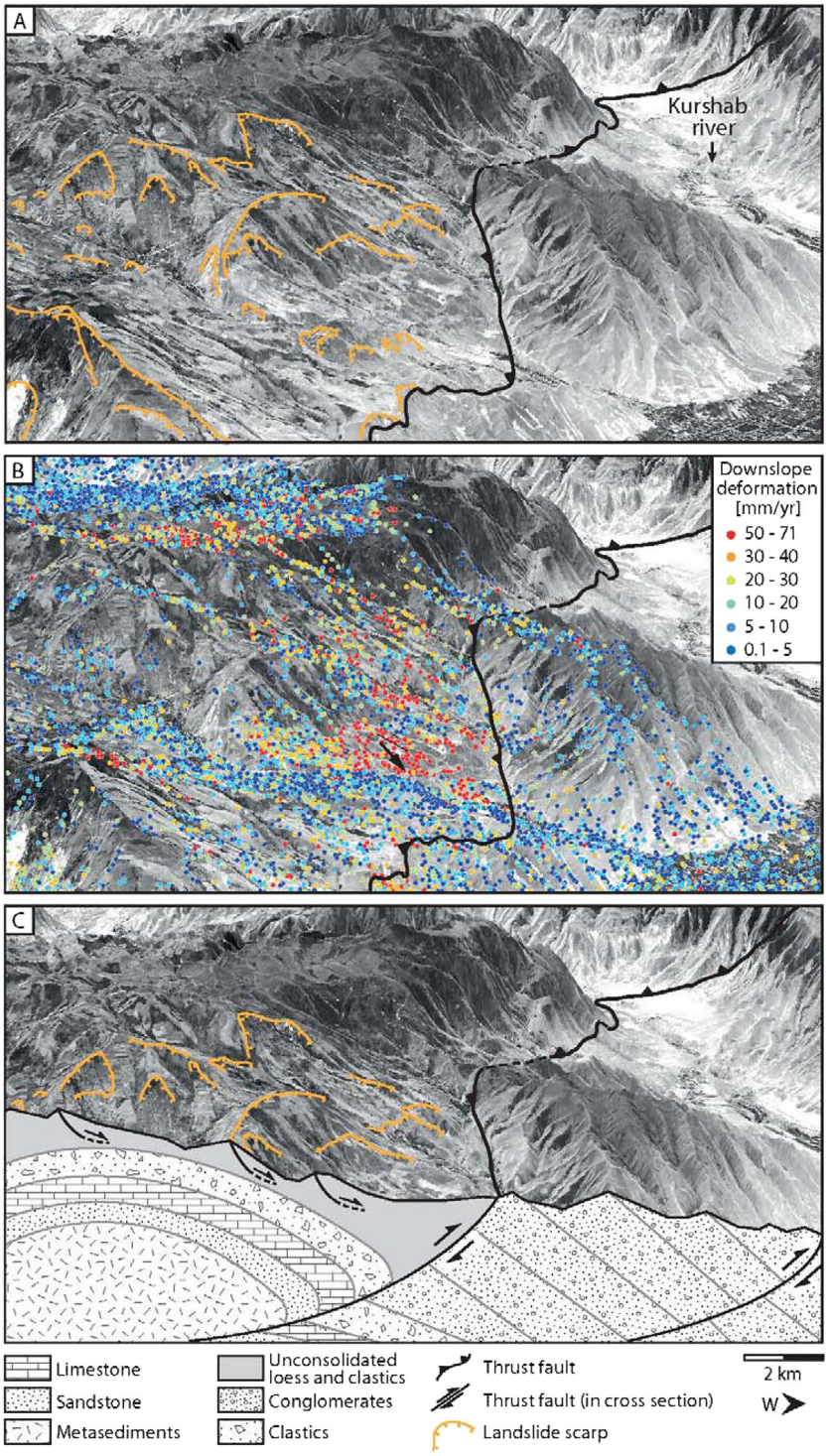

Figure 9. Oblique 3D view of hotspot cluster 1 (Figures 3 and 4) based on optical RapidEye satellite data acquired in August 2014 with: (a) mapped landslide areas and scarps; (b) downslope deformation rates; and (c) simplified geological cross-section. Cross-section reveals that landsliding associated with cluster 1 occurs along cataclinal slopes in the hanging wall of folded, poorly lithified Miocene clastic sedimentary rocks and Cretaceous limestones and sandstones. [Colour figure can be viewed at wileyonlinelibrary.com]

© 2019 The Authors. Earth Surface Processes and Landforms Published by John Wiley & Sons Ltd

distribution of the observed deformation velocities in the context of elevation, slope angle and slope-movement direction at our analysed sites revealed that the sites of deformation did not depend in priority on the steepness of the terrain, but were determined by lithology, active faults and tectonics (Dramis and Sorriso-Valvo, 1994; Agliardi *et al.*, 2001). There was a clear correlation between the tectonically controlled dip of the bedding planes in the hanging and footwalls of active folds and faults that locate deep mass creep. Hotspot cluster 1 was characterized by cataclinal slopes (Figures 7 and 11) that were associated with an active thrust fault (Figures 2 and 4). Strom and Korup (2006) argued that many of the large rock-slope failures in the Kyrgyz Tien Shan Mountains occurred on slopes truncated by active faults. The temporal evolution of the detected deformations during 2007–2010 indicated continuous movements in the LOS direction with a distinct peak in October 2008 along cluster 1, which was initiated by the 26 September 2008 Mw 4.1 earthquake (Teshebaeva *et al.*, 2015).

The majority of landslides developed within DSGSD presented slow movements. Although we did not have a longer time-series of moving DSGSD and landslides in this region, our observations suggested that at least some of the larger

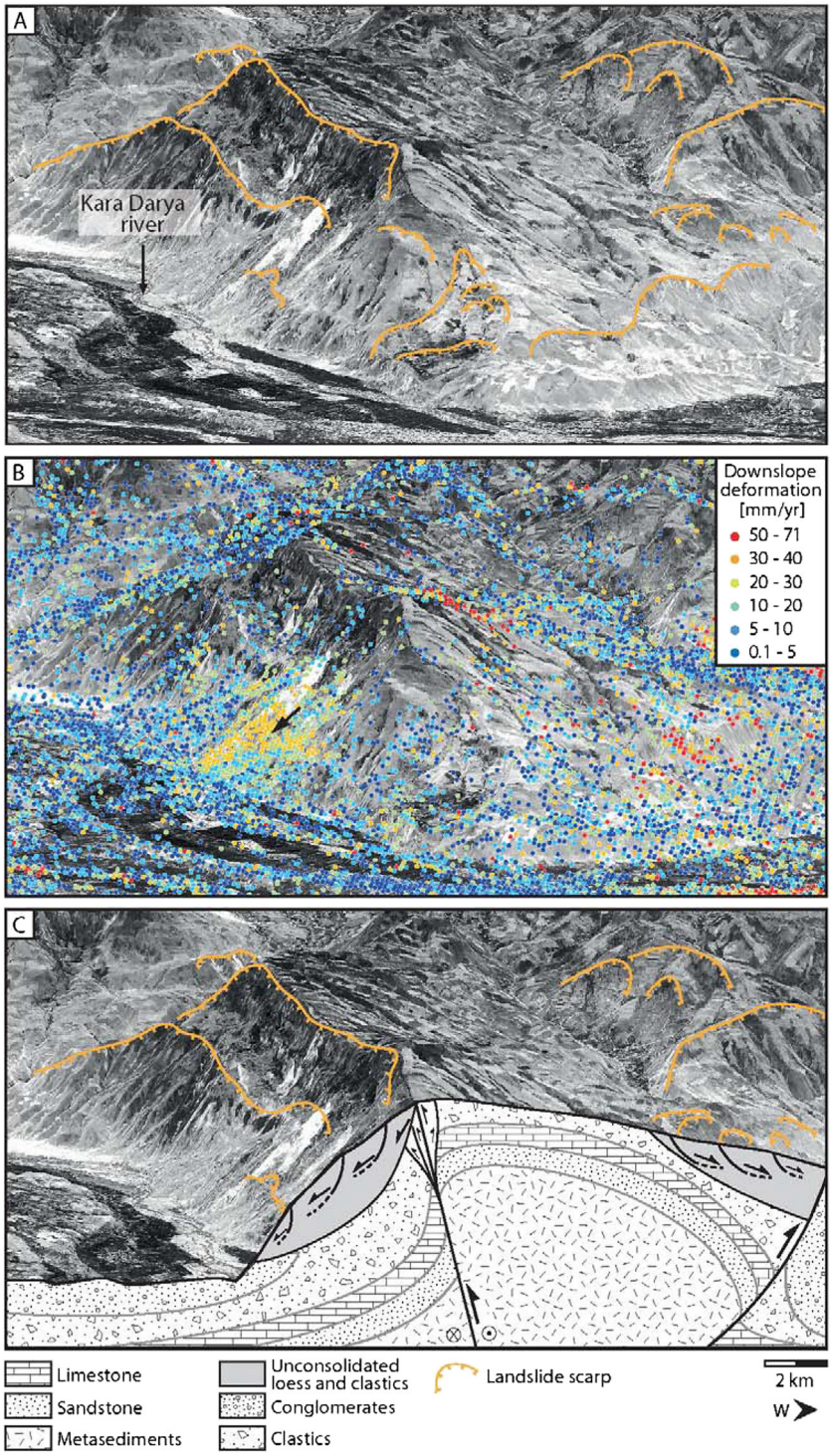

Figure 10. Oblique 3D view of cluster 2 (Figures 3 and 4) based on optical RapidEye satellite data acquired in August 2014 with: (a) mapped landslide areas and scarps; (b) downslope deformation rates; and (c) simplified geological cross-section. Cross-section reveals that landsliding in cluster 2 is associated with anaclinal slopes in hanging and footwalls of reverse and dextrally oblique reverse faults, respectively. Rock types are the same as in Figure 8. Note proximity of river channel with respect to toe section of landslide body. [Colour figure can be viewed at wileyonlinelibrary.com]

© 2019 The Authors. Earth Surface Processes and Landforms Published by John Wiley & Sons Ltd

landslide mass movements were associated with protracted motion and active inverse faulting (Figure 6). However, it is conceivable that deep-seated masses were slowly creeping, given the close association of faults and folds with the actively deforming slopes. These unconsolidated clastic sediments superseding the massif and plastically deforming limestones were being detached to form the landslides (Figure 11). Moderate seismicity was supplementary trigger of these mass movements in the area (Figures 1 and 6). The slope instability in hotspot cluster 2 was characterized by anaclinal slopes associated with the upward-tilted footwall of a dextrally oblique reverse fault and the limb of a hanging-wall anticline (Figures 7 and 11). The DSGSD surface breakaway scarps coincided with the surface expression of the wide fault gouge zone at cluster 2, whereas this relationship did not exist in the hanging-wall anticline (Figure 10). Both investigated DSGSD settings were associated with tectonically active structures that preconditioned the involved rock masses for failure, which included breakaway zones. However, in addition to the structural conditions, the deforming lithologies were composed of unconsolidated clastic sediments above massive Cretaceous–Paleogene limestones and sediments that constituted alternating weak zones, and these were potentially more prone to additional detachment horizons in highly anisotropic sequences (Figures 9 and 10).

Downslope movement of the DSGSD in both hotspot cluster areas was facilitated by the deformed, slope-parallel bedding planes that dipped toward lower sectors in the topography (Figure 9), and the mechanical weakness of the involved strata (Figures 10 and 11). The spatial distribution of the DSGSD signals

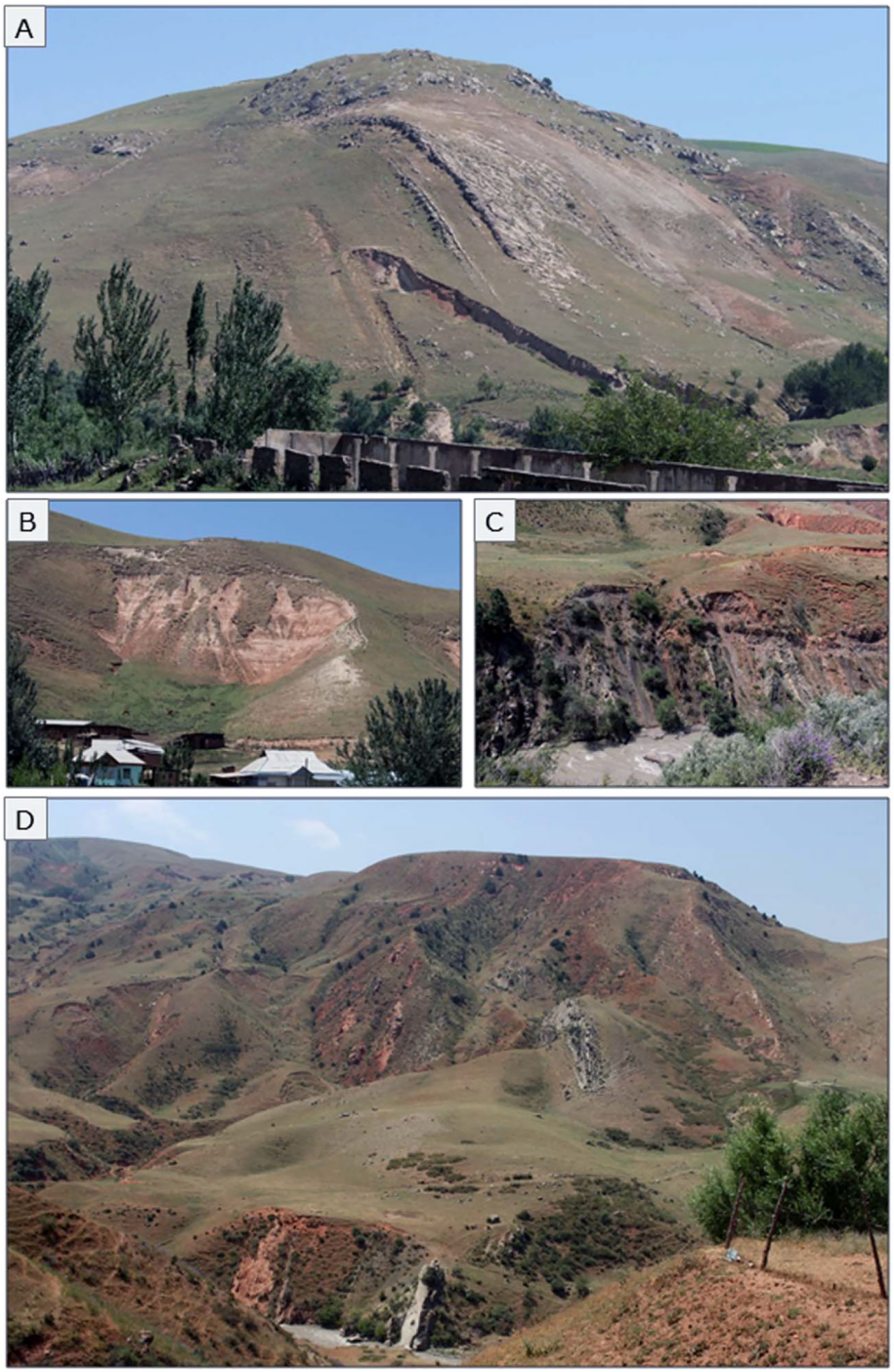

Figure 11. Different field views of cataclinal and anaclinal slopes: (A, B) cataclinal slopes from cluster 1 area; (C, D) anaclinal slopes from cluster 2 area. [Colour figure can be viewed at wileyonlinelibrary.com]

© 2019 The Authors. Earth Surface Processes and Landforms Published by John Wiley & Sons Ltd

on clusters 1 and 2 was close to active tectonic features with moderate seismicity. Our InSAR-defined kernel density and local seismicity kernel density estimation (Figures 4 and 6) corresponded to the same location that strengthened our interpretation. The areas of seismic strain release and InSAR signals correlated clearly and, therefore, underlined that (1) the inherited tectonic structures of slopes strongly influenced localization of DSGSD and (2) seismic activity led to gravitational destabilization or reactivation of slopes (Jibson *et al.*, 2004; Moro *et al.*, 2007; Jomard *et al.*, 2014). DSGSD-triggered processes, such as slope steepening and de-buttressing after deglaciation, which have been suggested for some regions in Italy (Agliardi *et al.*, 2001), were an unlikely mechanism for our study area in Tien Shan (Strom and Korup, 2006); Tien Shan is located at altitudes and in mountain ranges with more foothill character where glaciers never existed.

We searched for a possible correlation between the patterns that were observed in the displacement time series and precipitation. Our 4-year observation period did not reveal a direct relationship between the rate of slope movement and precipitation (Teshebaeva *et al.*, 2015). Nevertheless, in future studies decadal InSAR time series may help to elucidate such potential relationships. In addition to seismic triggering, a key question for future work in this context is: (1) do extreme rainfall events affect this region, (2) do the landslides developed within slow-moving DSGSD have the potential to accelerate within catastrophic dimensions? These issues are especially important in the context of global environmental change and predicted changes in the spatiotemporal characteristics of precipitation regimes (Nearing *et al.*, 2004). Using a new approach in long-term InSAR monitoring and active deformation along mountain front, our work contributes to an improved natural risk assessment in such structures.

Conclusions

In this study, we documented results from InSAR and combined geomorphological and tectonic investigations of a segment of the Alai Range front in the south-west Kyrgyz Tien Shan Mountains. This mountain front is an integral part of an active fold-and-thrust belt with WSW–ENE-striking and SSE-dipping thrust and reverse faults and with NW–SE-striking conjugate faults. Numerous active mass movements that are located near tectonically active structures affect hillslopes of the Alai Range. We analysed hillslope instabilities using InSAR time-series data combined with digital topography and field observations of surface dynamics and tectonic geomorphology. Our new InSAR time-series data, combined with spatial cluster analysis, revealed two areas of continuous downslope-moving areas of the mountain flanks. In these zones, the gemorphology results and field observations allowed us to identify the surface ruptures of DSGSD as very closely related to active deformation along a contracting mountain front.

The deformation rates of these sectors exposed no clear correlation with elevation, hillslope angle or drainage system. We applied a conformity analysis to test for other forcing factors to explain the spatial distribution of hillslope deformation. The very high degree of conformity between topography and bedding planes of the sedimentary strata exposed at the mountain fronts showed that the spatial distribution of downslope deformation was mainly controlled by the geometry of the folded and faulted structures and their lithology. Therefore, we conclude that active tectonics associated with folded and faulted specific anisotropic sedimentary sequences precondition the processes of DSGSD and sustain the rates of slow-moving mass creep at depth in the south Tien Shan Mountains.

Acknowledgements—The authors do not have any conflicts of interest to declare. We thank Oliver Korup, Sigrid Roessner and Bolot Moldobekov for valuable comments and feedback on this manuscript, which helped to improve our work. This research was funded by the Volkswagen Foundation within the framework of the LUCA (Land Use, Ecosystem Services and Human Welfare in Central Asia) postgraduate programme. The Central Asia and Afghanistan Research Fellowship, the University of Central Asia and the German Research Foundation under the auspices of the Graduate School GRK1364 'Shaping Earth's Surface in a variable Environment' (Strecker STR 373/18-1) also supported this study. Additional financial support was provided by the CAWa project, which was funded by the German Federal Foreign Office as part of the German Water Initiative for Central Asia. The ALOS data for this study were provided by research proposal P610 funded by the Japanese Aerospace Agency.

References

Abdrakhmatov K, Havenith HB, Delvaux D, Jongmans D, Trefois P. 2003. Probabilistic PGA and Arias Intensity maps of Kyrgyzstan (Central Asia). *Journal of Seismology* **7**(2): 203. https://doi.org/10.1023/A:1023559932255.

Agliardi F, Crosta G, Zanchi A. 2001. Structural constraints on deep-seated slope deformation kinematics. *Engineering Geology* **59**(1–2): 83–102. https://doi.org/10.1016/S0013-7952(00)00066-1.

Agliardi F, Crosta GB, Frattini P, Malusà MG. 2013. Giant non-catastrophic landslides and the long-term exhumation of the European Alps. *Earth and Planetary Science Letters* **365**: 263–274. https://doi.org/10.1016/j.epsl.2013.01.030.

Ambrosi C, Crosta GB. 2006. Large sackung along major tectonic features in the Central Italian Alps. *Engineering Geology* **83**(1–3): 183–200. https://doi.org/10.1016/j.enggeo.2005.06.031.

Arrowsmith JR, Strecker MR. 1999. Seismotectonic range-front segmentation and mountain-belt growth in the Pamir-Alai region, Kyrgyzstan (India-Eurasia collision zone). *Bulletin of the Geological Society of America* **111**(11): 1665–1683. https://doi.org/10.1130/0016-7606(1999)111<1665:SRFSAM>2.3.CO;2.

Bazhenov ML, Burtman VS, Dvorova AV. 1999. Permian paleomagnetism of the Tien Shan fold belt, Central Asia: post-collisional rotations and deformation. *Tectonophysics* **312**(2–4): 303–329. https://doi.org/10.1016/S0040-1951(99)00181-X.

Berardino P, Fornaro G, Lanari R, Sansosti E. 2002. A new algorithm for surface deformation monitoring based on small baseline differential SAR interferograms. *IEEE Transactions on Geoscience and Remote Sensing* **40**(11): 2375–2383. https://doi.org/10.1109/TGRS.2002.803792.

Biske YS, Konopelko DL, Shergina JP, Kusnetsov LV, Rublev AG. 1996. The age and tectonic setting of Hercynian granitoids of the Kokshaal segment, south Tien-Shan. In *Vestnik - Sankt-Peterburgskogo Universiteta*. Geologiya i Geografiya: Seriya.

Burtman BS. 2006. The Tien Shan Early Paleozoic tectonics and geodynamics. *Russian Journal of Earth Sciences* **8**(3): 1–23. https://doi.org/10.2205/2006es000202.

Burtman VS, Molnar P. 1993. Geological and geophysical evidence for deep subduction of continental crust beneath the Pamir. In *GSA Special Papers*, Vol. 281. Geological Society of America: Boulder, CO; 1–76.

Buslov MM, De Grave J, Bataleva EAV, Batalev VY. 2007. Cenozoic tectonic and geodynamic evolution of the Kyrgyz Tien Shan Mountains: a review of geological, thermochronological and geophysical data. *Journal of Asian Earth Sciences* **29**(2–3): 205–214. https://doi.org/10.1016/j.jseaes.2006.07.001.

Capitani M, Ribolini A, Federici PR. 2013. Influence of deep-seated gravitational slope deformations on landslide distributions: a statistical approach. *Geomorphology* **201**: 127–134. https://doi.org/10.1016/j.geomorph.2013.06.014.

Cascini L, Fornaro G, Peduto D. 2010. Advanced low- and full-resolution DInSAR map generation for slow-moving landslide analysis at different scales. *Engineering Geology* **112**(1–4): 29–42. https://doi.org/10.1016/j.enggeo.2010.01.003.

Chediya OK. 1986. *Morphostructure and Neo-tectonics of the Tien Shan*. Frunze: Academia Nauk Kyrgyz CCP; 313.

© 2019 The Authors. Earth Surface Processes and Landforms Published by John Wiley & Sons Ltd

Cobbold PR, Sadybakasov E, Thomas JC. 1992. Cenozoic transpression and basin development, Kyrghyz Tienshan, Central Asia. In *Geodynamic Evolution of Sedimentary Basins, International Symposium*, Roure F, Ellouz N, Shein VS, Skvortsov I (eds); 181–202.

Colesanti C, Wasowski J. 2006. Investigating landslides with space-borne Synthetic Aperture Radar (SAR) interferometry. *Engineering Geology* **88**(3–4): 173–199. https://doi.org/10.1016/j.enggeo.2006.09.013.

Coutand I, Strecker MR, Arrowsmith JR, Hilley G, Thiede RC, Korjenkov A, Omuraliev M. 2002. Late Cenozoic tectonic development of the intramontane Alai Valley (Pamir-Tien Shan region, central Asia): an example of intracontinental deformation due to the Indo-Eurasia collision. *Tectonics* **21**(6): 3-1–3-19. https://doi.org/10.1029/2002TC001358.

Crosta GB, di Prisco C, Frattini P, Frigerio G, Castellanza R, Agliardi F. 2013. Chasing a complete understanding of the triggering mechanisms of a large rapidly evolving rockslide. *Landslides* **11**(5): 747–764. https://doi.org/10.1007/s10346-013-0433-1.

Cruden DM, Hu XQ. 1996. Hazardous modes of rock slope movement in the Canadian rockies. *Environmental and Engineering Geoscience* **2**(4): 507–516. https://doi.org/10.2113/gseegeosci.II.4.507.

Danneels G, Bourdeau C, Torgoev I, Havenith HB. 2008. Geophysical investigation and dynamic modelling of unstable slopes: case-study of Kainama (Kyrgyzstan). *Geophysical Journal International* **175**(1): 17–34. https://doi.org/10.1111/j.1365-246X.2008.03873.x.

Delgado J, Vicente F, García-Tortosa F, Alfaro P, Estévez A, Lopez-Sanchez JM, Tomás R, Mallorquí JJ. 2011. A deep seated compound rotational rock slide and rock spread in SE Spain: structural control and DInSAR monitoring. *Geomorphology* **129**(3–4): 252–262. https://doi.org/10.1016/j.geomorph.2011.02.019.

Dikau R, Brunsden D, Schrott L, Ibsen ML. 1996. *Landslide Recognition: Identification, Movement and Causes*. International Association of Geomorphologists, Publication No. 5. Wiley: Chichester; 251.

Dramis F, Sorriso-Valvo M. 1994. Deep-seated gravitational slope deformations, related landslides and tectonics. *Engineering Geology* **38**(3–4): 231–243. https://doi.org/10.1016/0013-7952(94)90040-X.

Duethmann D, Zimmer J, Gafurov A, Güntner A, Kriegel D, Merz B, Vorogushyn S. 2013. Evaluation of areal precipitation estimates based on downscaled reanalysis and station data by hydrological modelling. *Hydrology and Earth System Sciences* **9**(9): 10719–10773. https://doi.org/10.5194/hess-17-2415-2013.

Farr TG, Kobrick M. 2000. Shuttle radar topography mission produces a wealth of data. *Eos* **81**(48): 583–585. https://doi.org/10.1029/EO081i048p00583.

Feld C, Haberland C, Schurr B, Sippl C, Wetzel HU, Roessner S, Ickrath M, Abdybachaev U, Orunbaev S. 2015. Seismotectonic study of the Fergana Region (Southern Kyrgyzstan): distribution and kinematics of local seismicity. *Earth, Planets and Space* **67**: 40. https://doi.org/10.1186/s40623-015-0195-1.

Galadini F. 2006. Quaternary tectonics and large-scale gravitational deformations with evidence of rock-slide displacements in the Central Apennines (central Italy). *Geomorphology* **82**(3–4): 201–228. https://doi.org/10.1016/j.geomorph.2006.05.003.

Getis A, Ord JK. 2010. The analysis of spatial association by use of distance statistics. In *Perspectives on Spatial Data Analysis*, Anselin L, Rey S (eds). Springer: Berlin; 127–145.

Ghose S, Hamburger MW, Ammon CJ. 1998. Source parameters of moderate-sized earthquakes in the Tien Shan, Central Asia from regional moment tensor inversion. *Geophysical Research Letters* **25**(16): 3181–3184. https://doi.org/10.1029/98GL02362.

Goldstein RM, Werner CL. 1998. Radar interferogram filtering for geophysical applications. *Geophysical Research Letters* **25**(21): 4035–4038. https://doi.org/10.1029/1998GL900033.

Gori S, Falcucci E, Dramis F, Galadini F, Galli P, Giaccio B, Messina P, Pizzi A, Sposato A, Cosentino D. 2014. Deep-seated gravitational slope deformation, large-scale rock failure, and active normal faulting along Mt. Morrone (Sulmona basin, Central Italy): geomorphological and paleoseismological analyses. *Geomorphology* **208**: 88–101. https://doi.org/10.1016/j.geomorph.2013.11.017.

Haberland C, Abdybachaev U, Schurr B, Wetzel HU, Roessner S, Sarnagoev A, Orunbaev S, Janssen C. 2011. Landslides in southern Kyrgyzstan: understanding tectonic controls. *Eos* **92**(20): 169–170. https://doi.org/10.1029/2011EO200001.

Havenith HB, Torgoev I, Meleshko A, Alioshin Y, Torgoev A, Danneels G. 2006. Landslides in the Mailuu-Suu Valley, Kyrgyzstan – hazards and impacts. *Landslides* **3**(2): 137–147. https://doi.org/10.1007/s10346-006-0035-2.

Havenith HB, Strom A, Calvetti F, Jongmans D. 2010. Seismic triggering of landslides. Part B: Simulation of dynamic failure processes. *Natural Hazards and Earth System Sciences* **3**: 663–682. https://doi.org/10.5194/nhess-3-663-2003.

Hermanns RL, Niedermann S, Villanueva Garcia A, Gomez JS, Strecker MR. 2001. Neotectonics and catastrophic failure of mountain fronts in the southern intra-Andean Puna Plateau, Argentina. *Geology* **29**(7): 619–623. https://doi.org/10.1130/0091-7613(2001)029<0619:NACFOM>2.0.CO;2.

Hilley GE, Bürgmann R, Ferretti A, Novali F, Rocca F. 2004. Dynamics of slow-moving landslides from permanent scatterer analysis. *Science* **304**(5679): 1952–1955. https://doi.org/10.1126/science.1098821.

Hooper AJ. 2008. A multi-temporal InSAR method incorporating both persistent scatterer and small baseline approaches. *Geophysical Research Letters* **35**(16). https://doi.org/10.1029/2008GL034654.

Hooper A, Zebker HA. 2007. Phase unwrapping in three dimensions with application to InSAR time series. *JOSA* **24**(9): 2737–2747.

Hungr O, Leroueil S, Picarelli L. 2014. The Varnes classification of landslide types, an update. *Landslides* **11**(2): 167–194. https://doi.org/10.1007/s10346-013-0436-y.

Ibatulin C. 2011. *Monitoring of Landslides in Kyrgyzstan*. Ministry of Emergency Situations of the Kyrgyz Republic: Bishkek; 145.

Jibson RW, Harp EL, Schulz W, Keefer DK. 2004. Landslides triggered by the 2002 Denali fault, Alaska, earthquake and the inferred nature of the strong shaking. *Earthquake Spectra* **20**(3): 669–691. https://doi.org/10.1193/1.1778173.

Jomard H, Lebourg T, Guglielmi Y. 2014. Morphological analysis of deep-seated gravitational slope deformation (DSGSD) in the western part of the Argentera massif. A morpho-tectonic control? *Landslides* **11**(1): 107–117. https://doi.org/10.1007/s10346-013-0434-0.

Kampes BM, Hanssen RF, Perski Z. 2003. *Radar interferometry with public domain tools*. In Proceedings of FRINGE (Vol. 3).

Keefer DK. 1984. Landslides caused by earthquakes. *Geological Society of America Bulletin* **95**: 406–421. https://doi.org/10.1130/0016-7606(1984)95<406:LCBE>2.0.CO;2.

Klose M, Highland L, Damm B, Terhorst B. 2014. Estimation of direct landslide costs in industrialized countries: challenges, concepts, and case study. In *Landslide Science for a Safer Geoenvironment, Vol. 2: Methods of Landslide Studies*, Sassa K, Canuti P, Yin Y (eds). Springer: Berlin; 661–667.

Landgraf A, Dzhumabaeva A, Abdrakhmatov KE, Strecker MR, Macaulay EA, Arrowsmith JR, Sudhaus H, Preusser F, Rugel G, Merchel S. 2016. Repeated large-magnitude earthquakes in a tectonically active, low-strain continental interior: the northern Tien Shan, Kyrgyzstan. *Journal of Geophysical Research: Solid Earth* **121**(5): 3888–3910. https://doi.org/10.1002/2015JB012714.

Meentemeyer RK, Moody A. 2000. Automated mapping of conformity between topographic and geological surfaces. *Computers and Geosciences* **26**(7): 815–829. https://doi.org/10.1016/S0098-3004(00)00011-X.

Molnar P, Tapponnier P. 1975. Cenozoic tectonics of Asia: effects of a continental collision. *Science* **189**(4201): 419–426. https://doi.org/10.1126/science.189.4201.419.

Moro M, Saroli M, Salvi S, Stramondo S, Doumaz F. 2007. The relationship between seismic deformation and deep-seated gravitational movements during the 1997 Umbria–Marche (Central Italy) earthquakes. *Geomorphology* **89**(3–4): 297–307. https://doi.org/10.1016/j.geomorph.2006.12.013.

Nearing MA, Pruski FF, O'Neal MR. 2004. Expected climate change impacts on soil erosion rates: a review. *Journal of Soil and Water Conservation* **59**(1): 43–50.

Qiu H, Regmi AD, Cui P, Cao M, Lee J, Zhu X. 2016. Size distribution of loess slides in relation to local slope height within different slope morphologies. *Catena* **145**: 155–163. https://doi.org/10.1016/j.catena.2016.06.005.

© 2019 The Authors. Earth Surface Processes and Landforms Published by John Wiley & Sons Ltd

Reigber C, Michel GW, Galas R, Angermann D, Klotz J, Chen JY, Papschev A, Arslanov R, Tzurkov VE, Ishanov MC. 2001. New space geodetic constraints on the distribution of deformation in Central Asia. *Earth and Planetary Science Letters* **191**(1–2): 157–165. https://doi.org/10.1016/S0012-821X(01)00414-9.

Roessner S, Wetzel H, Kaufmann H, Potsdam G, Sensing SR, Potsdam D. 2000. Landslide investigations in southern Kyrgyzstan based on a digital elevation model derived from stereoscopic MOMS-2P data. *International Archives of Photogrammetry and Remote Sensing* **XXXIII**(B7): 1259–1266.

Roessner S, Wetzel HU, Kaufmann H, Sarnagoev A. 2005. Potential of satellite remote sensing and GIS for landslide hazard assessment in Southern Kyrgyzstan (Central Asia). *Natural Hazards* **35**(3): 395–416. https://doi.org/10.1007/s11069-004-1799-0.

Rosen PA, Hensley S, Peltzer G, Simons M. 2004. Updated repeat orbit interferometry package released. *Eos* **85**(5): 47. https://doi.org/10.1029/2004EO050004.

Schurr B, Ratschbacher L, Sippl C, Gloaguen R, Yuan X, Mechie J. 2014. Seismotectonics of the Pamir. *Tectonics* **33**(8): 1501–1518. https://doi.org/10.1002/2014TC003576.

Silverman BW. 1986. Density Estimation for Statistics and Data Analysis. Chap and Hall.

Sobel ER, Schoenbohm LM, Chen J, Thiede R, Stockli DF, Sudo M, Strecker MR. 2011. Late Miocene–Pliocene deceleration of dextral slip between Pamir and Tarim: implications for Pamir orogenesis. *Earth and Planetary Science Letters* **303**(3–4): 369–378. https://doi.org/10.1016/j.epsl.2011.02.012.

Sousa A, Pereira F, Sousa JJ, Patrício G, Magalhães L, Ruiz AM, Guimarães P. 2014. viStaMPS – a collaborative project for StaMPS-MTI results interpretation. *Procedia Technology* **16**: 842–848. https://doi.org/10.1016/j.protcy.2014.10.034.

Stramondo S, Saroli M, Tolomei C, Moro M, Doumaz F, Pesci A, Loddo F, Baldi P, Boschi E. 2007. Surface movements in Bologna (Po Plain - Italy) detected by multitemporal DInSAR. *Remote Sensing of Environment* **110**(3): 304–316. https://doi.org/10.1016/j.rse.2007.02.023.

Strecker MR, Hilley GE, Arrowsmith JR, Coutand I. 2003. Differential structural and geomorphic mountain-front evolution in an active continental collision zone: the northwest Pamir, southern Kyrgyzstan. *Bulletin of the Geological Society of America* **115**(2): 166–181. https://doi.org/10.1130/0016-7606(2003)115<0166:DSAGMF>2.0.CO;2.

Strom A. 2013. Geological prerequisites for landslide dams' disaster assessment and mitigation in Central Asia. In *Progress of Geo-Disaster Mitigation Technology in Asia*, Wang F, Miyajima M, Li T, Shan W, Fathani TF (eds). Springer: Berlin; 17–53.

Strom A. 2015. Clustering of large bedrock landslides and recurrent slope failure: implications for land seismic hazard assessment of the Tien Shan-Djungaria region. *International Journal of Geohazards and Environment* **1**(3): 110–121.

Strom AL, Korup O. 2006. Extremely large rockslides and rock avalanches in the Tien Shan Mountains, Kyrgyzstan. *Landslides* **3**(2): 125–136. https://doi.org/10.1007/s10346-005-0027-7.

Sycheva NA, Yunga SL, Bogomolov LM, Makarov VI. 2008. Seismotectonic deformations and recent tectonics of the Tien Shan. *Izvestiya, Physics of the Solid Earth* **44**(5): 351–363. https://doi.org/10.1134/s1069351308050017.

Taylor M, Yin A. 2009. Active structures of the Himalayan-Tibetan orogen and their relationships to earthquake distribution, contemporary strain field, and Cenozoic volcanism. *Geosphere* **5**(3): 199–214. https://doi.org/10.1130/ges00217.1.

Teshebaeva K, Sudhaus H, Echtler H, Schurr B, Roessner S. 2014, 198. Strain partitioning at the eastern Pamir-Alai revealed through SAR data analysis of the 2008 Nura earthquake. *Geophysical Journal International* (2): 760–774. https://doi.org/10.1093/gji/ggu158.

Teshebaeva K, Roessner S, Echtler H, Motagh M, Wetzel H-U, Molodbekov B. 2015. ALOS/PALSAR InSAR time-series analysis for detecting very slow-moving landslides in Southern Kyrgyzstan. *Remote Sensing* **7**: 8973–8994. https://doi.org/10.3390/rs70708973.

Tolomei C, Taramelli A, Moro M, Saroli M, Aringoli D, Salvi S. 2013. Analysis of the deep-seated gravitational slope deformations over Mt. Frascare (Central Italy) with geomorphological assessment and DInSAR approaches. *Geomorphology* **201**: 281–292. https://doi.org/10.1016/j.geomorph.2013.07.002.

Wetzel H-U, Roessner S, Sarnagoev A. 2000. Remote sensing and CIS based geological mapping for assessment of landslide hazard in Southern Kyrgyzstan (Central Asia). In *Management Information Systems 2000 - GIS and Remote Sensing*, Brebbia C, Pascolo P (eds). WIT Press: Southampton; 355–366.

Yerokhin S. 1999. *Investigation of Landslide Occurence in Osh and Djalalabad Provinces of the Kyrgyz Republic*. Bishkek: Institute of Geology.

Zhao C, Lu Z, Zhang Q, de la Fuente J. 2012. Large-area landslide detection and monitoring with ALOS/PALSAR imagery data over Northern California and Southern Oregon, USA. *Remote Sensing of Environment* **124**: 348–359. https://doi.org/10.1016/j.rse.2012.05.025.

Zubovich AV, Wang X-Q, Scherba YG, Schelochkov GG, Reilinger R, Reigber C, Mosienko OI, Molnar P, Michajljow W, Makarov VI, Li J, Kuzikov SI, Herring TA, Hamburger MW, Hager BH, Dang Y-M, Bragin VD, Beisenbaev RT. 2010. GPS velocity field for the Tien Shan and surrounding regions. *Tectonics* **29**(6): TC6014. https://doi.org/10.1029/2010TC002772.

© 2019 The Authors. Earth Surface Processes and Landforms Published by John Wiley & Sons Ltd